Fractal description of fouling deposits in boiling heat transfer modelling

T. Dupuy, T. Prusek, F. Oukacine, M. Lacroix, A. Kaiss, J.P. Clerc, Marc Jaeger

Fractal description of fouling deposits in boiling heat transfer modelling

T. Dupuy[a,b,*], T. Prusek[a], F. Oukacine[a], M. Lacroix[c], A. Kaiss[d], J.P. Clerc[d], M. Jaeger[b]

[a] *EDF-R&D Center, Chatou, France*
[b] *Aix Marseille University, CNRS, Centrale Marseille, M2P2, UMR 7340, Marseille, France*
[c] *University of Sherbrooke, Faculty of Engineering, Sherbrooke, Canada*
[d] *Aix Marseille University, CNRS, IUSTI, UMR 7343, Marseille, France*

Abstract

A novel methodology is developed for predicting the thermal impact of fouling in Steam Generators (SG). The originality of this methodology is to resort to fractal and statistical theories to depict the porous structure of the deposits. The proposed Statistical Fractal methodology (SF) accounts for the heat transfer driven by the liquid-vapor phase change inside the deposits. It simulates the complex intricate networks of sinuous open pores of different scales, with liquid inflows (capillaries) and vapor outflows (steam-chimneys). The multi-layered representation of fouling deposits allows to mimic aging mechanisms such as densification which occur during SG operation.

The SF predictions are consistent with experimental data. The deposit thickness and the profile of porosity are found to be the most influential fouling properties on the heat exchange. The methodology is capable to simulate the experimentally observed heat transfer enhancement for thin and porous deposit as well as the heat exchange decline for thick and dense deposit.

Keywords: Fouling, porous media, fractal, boiling heat transfer, heat exchanger

2010 MSC: 00-01, 99-00

*Corresponding author. *E-mail address:* thibaut.dupuy@edf.fr

1. Introduction

Fouling refers to the unwanted deposition of material from a flow stream on a surface. For example, in nuclear power plants, fouling may stem from the deposition of corrosion products like magnetite (Fe_3O_4) on the surfaces of the shell and of the tubes of Steam Generators (SG).

Fouling is usually detrimental to the heat transfer processes. As a result, the overall thermal performance of the heat exchanger declines. To alleviate this problem, the heat transfer equipment must be regularly cleaned. The cleaning is usually carried out by mechanical or chemical means. But in the broad context of the power and process industry, this maintenance action is complex, time consuming, and expensive. It must be carefully planned and executed for a successful outcome. This is why it is imperative to understand and to predict the fouling process.

The impact of fouling has been thoroughly investigated for deposits on nuclear reactor fuel rods named Chalk River Unidentified Deposits (CRUD). Cohen [1] developed a one-dimensional heat and mass transfer model in which the fouling deposits are split into two distinct regions: one deposit region is populated with small pores filled with liquid and the other is populated with chimneys filled with steam. Pan et al. [2] extended the work of Cohen by developing a two-dimensional (axial and radial) heat and momentum transfer model for porous deposits. Later, Short et Al. proposed a model that employs fractals to estimate the deposit properties in CRUD [3]. The energy and momentum equations are solved for two-dimensional steam chimneys surrounded by CRUD deposits. The chimneys are modelled as repeatable elements called fractals. More recently, Yeo and No [4] developed a heat transfer model that considers fouling deposits as a stack of two layers: in the top layer, the fluid is heated up to the saturation temperature and, in the bottom layer, boiling prevails. The boiling phenomenon is modelled with an empirical correlation. Similar to the

Short et al. model, a fractal approach was adopted to characterize the deposits and to estimate the deposit permeability.

In all the aforementioned studies however, the complexity of the microstructure of the fouling deposits on the heat transfer mechanisms was ignored. For example, the liquid-vapor circulation, which is dependent on the pore-size distribution of the fouling deposit, was not taken into account, nor was the percolation phenomenon.

On the other hand, Uhle [5] developed a one-dimensional model dedicated to the prediction of the fouling deposits in SG of nuclear power plants. In this model, the porous structure of the deposits is comprised of small and large pores. Both small pores and chimneys are allowed in the same deposit area and the porous structure is represented by a pore-size distribution function. Small pores are filled with liquid by capillary action whereas large pores are filled with vapor. Boiling occurs at the menisci between small and large pores.

Uhle's model has been relatively successful. But it suffers from two limitations. First, it relies on the pore-size distribution of the deposit. This physical property is, a priori, unknown. Moreover, it is difficult to measure. Second, the model assumes, wrongly, that the fluid is in a boiling state inside as well as outside the deposits all over the SG. The present paper remedies these limitations.

In the next section, the heat transfer equations are introduced and the effect of fouling is elucidated in terms of an overall heat transfer coefficient. The thermal conductivity and the permeability are developed in terms of the microstructural deposit properties in section 3. These thermal-hydraulic parameters are estimated with a novel fractal characterization methodology in section 4. The overall heat transfer model is then validated in section 6. Finally, the model is thoroughly tested and its predictions are discussed in section 7.

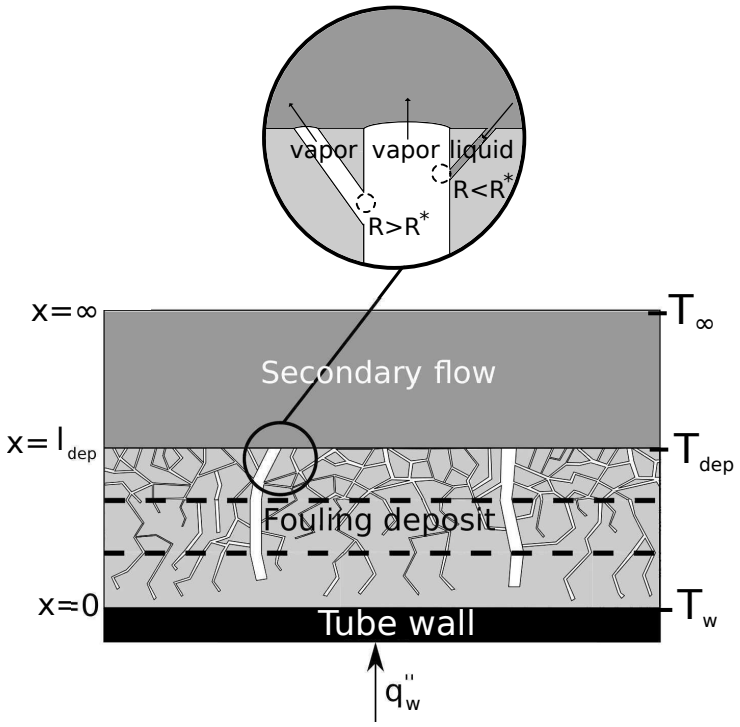

Figure 1: Schematics of the fouling deposit

2. Microscale heat transfer model for the deposit

The thermal performance of the fouled SG is assessed in terms of an overall heat transfer coefficient h_{fouled} defined as:

$$h_{fouled} = \frac{q_w^{''}}{T_w - T_\infty} \tag{1}$$

$q_w^{''}$ is the total heat flux from the surface of the SG-tubes to the flow stream. T_w is the temperature at the surface of the SG-tube and T_∞ is the mean temperature of the flow stream.

In order to estimate the overall heat transfer coefficient h_{fouled}, a one-dimensional (1D) microscale heat transfer model is developed for the deposit. This model can then be coupled to a full thermal-hydraulic code aimed at the numerical simulation of industrial steam generator. The term microscale refers

here to the scale of the fouling deposit whose thickness is of the order of micrometers. The temperatures T_w and T_∞ in Eq. 1 characterize the fluid-solid interface at the steam generator scale since the fouling deposit is too thin to be represented. However, at the microscale, the temperature in the deposit ranges from that at the surface of the tube wall to the temperature that prevails at the fluid-deposit interface. If x represents the radial distance from the tube wall, $T_w = T(x = 0)$ is the deposit temperature at the tube wall, $T_\infty = T(x \to \infty)$ is the mean temperature of the flow stream and $T_{dep} = T(x = l_{dep})$ is the deposit-fluid interface temperature for a deposit of thickness l_{dep}.

The total heat flux $q_w^{''}$ and the fluid temperature outside the deposit T_∞ are assumed to be known. They are inputs to the microscale model. The aim of the microscale model is to estimate the deposit temperature distribution $T(x)$ and therefore the temperature at the tube wall surface T_w. T_w is required for estimating the overall heat transfer coefficient h_{fouled} (Eq. 1). h_{fouled} takes into account the heat transfer through the deposit as well as the heat transfer at the deposit wetted surface. The originality of the present methodology is to combine an extension of Uhle's model [5] for the thermal-hydraulic behavior with a fractal approach that represents the microstructure of the fouling deposit. The fractal model enables the characterization of the complex fouling deposit structure with a minimum number of measurable parameters. Moreover, the present heat transfer deposit model accounts for the percolation phenomenon.

Uhle's model is one-dimensional in the x-direction ($x \in [0, l_{dep}]$). It considers the fouling deposit as a porous matrix in which the bulk fluid can enter in liquid phase, evaporate, and escape in vapor phase (Fig. 1). Uhle's model [5] rests on the following assumptions:

- The deposit is a porous matrix made of magnetite (Fe_3O_4). This assumption rests on experimental observations [6];
- The porous volume of the deposit is made of cylindrical pores. These pores obey to a statistical pore-size distribution φ;

- The liquid is in a saturated state inside and outside the deposits. It undergoes a liquid-vapor phase change in the deposit by absorbing the latent heat of vaporization H_B;

- The mass-flow rates entering and leaving the deposit are equal. Mass is conserved;

- The liquid-vapor interface is shaped as a meniscus of radius R^* (Fig. 1). The liquid-vapor interface allows to discriminate two types of pores: the pores whose radius is smaller than R^* are filled with liquid (capillaries) and the pores whose radius is larger than R^* are filled with vapor (steam chimneys).

The present methodology improves Uhle's model with the following three additional assumptions. These assumptions stem from observations made on industrial SG:

- The fouling deposit is made of superimposed layers of thickness Δx with different structural properties. The structural properties of the deposit are dependent on x. Indeed, measurements made on deposits [7],[8] revealed that layers near the tube surface are dense and layers near the fluid stream are porous. This internal structure may be attributed to the densification of the deposit layers over time;

- Some pores are closed and some are open. The proportion of open pores is dependent on the layer. Only open pores have a cylindrical shape and follow the statistical open pore-size distribution φ. Closed pores are small (their size is reduced by precipitation and clogging phenomena) and, as a result, they are filled with liquid only;

- The flow stream is not necessarily saturated outside the deposit. It is usually the case when it enters the steam generator.

Note that the thickness of the deposit l_{dep} is of the order of 100 μm. This number is small with respect to the steam generator tube radius R_{tube} which is

of the order of 1 cm. As a result, the equations for the 1-D microscale model can be laid out in terms of Cartesian coordinates (instead of radial coordinates). Furthermore, the following structural parameters for the deposits are defined (all surface areas are reported per unit length of tube):

- S_{dep} is the surface area occupied by the deposit layers. It is assumed to be constant;
- $S_p(x)$ is the surface area occupied by the pores for layer x;
- $\phi(x) = \dfrac{S_p(x)}{S_{dep}}$ is the surface fraction of pores at layer x. It represents the surface porosity and it is assumed to be equal to the volumetric porosity in a deposit layer of thickness Δx;
- $S_{op}(R, x)$ is the surface occupied by the open pores with a radius less than R and for layer x;
- $S_{op}(x) = S_{op}(R \to +\infty, x)$ is the surface occupied by all the open pores for layer x;
- $S_m(x) = S_{dep} - S_{op}(x)$ is the surface occupied by the deposit matrix for layer x;
- $\phi_{op}(x) = \dfrac{S_{op}(x)}{S_{dep}}$ is the open porosity. It is the surface fraction of the open pores for layer x;
- $\varphi(R, x) = \dfrac{S_{op}(R, x)}{S_{op}(x)}$ is the cumulative open pore-size distribution.

Referring to these definitions, the surface occupied by the open pores with a radius R is given by:

$$\frac{\partial S_{op}(R,x)}{\partial R}\mathrm{d}R = S_{op}(x)\frac{\partial \varphi}{\partial R}\mathrm{d}R = \phi_{op}(x)S_{dep}\frac{\partial \varphi}{\partial R}\mathrm{d}R \tag{2}$$

The distinction between the open pores filled with liquid and the open pores filled with vapor can be obtained from the meniscus radius R^*:

- $S_{op}^{l}(x) = S_{op}(R^*, x) = S_{op}(x)\varphi(R^*, x)$ is the surface occupied by open pores filled with liquid;

- $S_{op}^{g}(x) = S_{op}(x) - S_{op}(R^*, x) = S_{op}(x)(1 - \varphi(R^*, x))$ is the surface occupied by open pores filled with vapor.

The deposit temperature T may be obtained from a boiling dominated energy balance for the deposit and the boundary conditions for the heat flux:

$$\boxed{\begin{cases} k_{dep}(x)\dfrac{\mathrm{d}^2T}{\mathrm{d}x^2} = \Pi_B(x) \\ -\,k_{dep}\dfrac{\mathrm{d}T}{\mathrm{d}x}\bigg|_{x=0} = q_w'' \\ -\,k_{dep}\dfrac{\mathrm{d}T}{\mathrm{d}x}\bigg|_{x=l_{dep}} = h_{dep}\left(T_{dep} - T_\infty\right) \end{cases}} \tag{3}$$

k_{dep} is the effective thermal conductivity of the deposit populated with pores which will be determined with the statistical fractal methodology (section 3.1). h_{dep} is the heat transfer coefficient between the deposit surface and the bulk fluid. It is obtained from a saturated/subcooled flow boiling correlation (Liu and Winterton's correlation [9]) for $T_{dep} > T_B$. For $T_{dep} < T_B$, a correlation for forced-convection heat transfer (Dittus-Boelter's correlation [10]) is invoked.

Π_B is a thermal sink term which corresponds to the boiling power density evacuated by the boiling phenomenon in the open pores. Using the volumetric boiling coefficient $\alpha_B(x)$, Π_B expresses as:

$$\Pi_B = \begin{cases} \alpha_B(x)\left(T(x) - T_B(x)\right), & \text{if } T(x) \geq T_B(x) \\ 0, & \text{else} \end{cases} \tag{4}$$

Note that the boiling temperature T_B is a function of the surrounding pressure and thus of x. α_B is given by the Kovalev's analytical correlation [11]:

$$\alpha_B(x) = C_{Kov}\phi_{op}(x)^2\,\frac{\varphi(R^*, x)}{\sqrt{R^*}}\int_{R^*}^{+\infty}\frac{1}{R}\frac{\partial\varphi}{\partial R}dR \tag{5}$$

C_{Kov} is a constant which depends on the physical properties of the liquid phase [11].

The volumetric phase change coefficient $\alpha_B(x)$ depends on the microstructure of the deposit since the aforementioned analytical correlation involves the fraction of open pores $\phi_{op}(x)$ and the cumulative open pore-size distribution $\varphi(R, x)$. This coefficient is also coupled to the hydraulics via the radius meniscus R^*. The latter is estimated from the Laplace's relation:

$$P_g(x) - P_l(x) = \frac{2\gamma}{R^*(x)} \tag{6}$$

$P_l(x)$ and $P_g(x)$ are the liquid and vapor pressures respectively. γ is the surface tension.

Assuming a steady state and modelling viscous friction with Darcy's law, the vapor pressure $P_g(x)$ and the liquid pressure $P_l(x)$ are estimated from the momentum balance equation for each phase:

$$\begin{cases} \dfrac{dP_l}{dx} = \dfrac{\mu_l}{K_l(x)} V_l \\ \dfrac{dP_g}{dx} = \dfrac{\mu_g}{K_g(x)} V_g \end{cases} \tag{7}$$

μ refers to the dynamic viscosity. K represents the permeability. The latter is a hydraulic structural property which will be determined with the statistical fractal methodology (section 3.2).

The Darcy vapor velocity V_g can be estimated since $\frac{\mathrm{d}V_g}{\mathrm{d}x}$ corresponds to the volume of vapor produced by the phase change between x and $x + \mathrm{d}x$. $V_g(x)$ is obtained from the solution of the following equation with the boundary condition $V_g(0) = 0$:

$$\rho_g H_B \frac{\mathrm{d}V_g}{\mathrm{d}x} = \Pi_B(x) \tag{8}$$

Note that H_B and ρ_g are dependent on the local thermal-hydraulic conditions, that is, they vary with respect to the x-coordinate.

The liquid velocity $V_l(x)$ is coupled to the vapor velocity $V_g(x)$ through the local mass conservation equation. Since both liquid and vapor Darcy velocities are set equal to zero at the surface of the tube ($V_l(0) = V_g(0) = 0$), we obtain:

$$V_l(x) = -\frac{\rho_g}{\rho_l} V_g(x) \tag{9}$$

This relation indicates that the liquid and the vapor flow in opposite directions inside the deposit (Fig 1).

The boundary condition used for the liquid pressure is:

$$P_l(l_{dep}) = P_\infty \tag{10}$$

For the vapor phase, Equation 6 with $x = l_{dep}$ is retained. The radius $R^*_{dep} = R^*(x = l_{dep})$ corresponds to the limit between capillaries and steam chimneys at the top layer $x = l_{dep}$. This limit is determined numerically from the statistical fractal methodology (section 4.3).

Note that in this heat and mass transfer, the contribution of the convective transport has been neglected. This assumption is mainly based on the value of Reynolds number, less than 1 due to the small radius of pores.

3. Effective thermal-hydraulic properties of the deposit

3.1. Effective thermal conductivity k_{dep}

The present thermal conductivity model is based on Zhu and Li's work [12]. It takes into account however, both liquid and vapor phases in the porous structure, the percolation phenomenon and the presence of open and closed pores in the porous structure of the deposit.

As in Uhle's model, it assumes that open pores with radii larger than R^* are filled with vapor (steam chimneys) and pores with radii smaller than R^* are filled with liquid water (capillaries). The overall conductive resistance is comprised of three paths (Fig. 2):

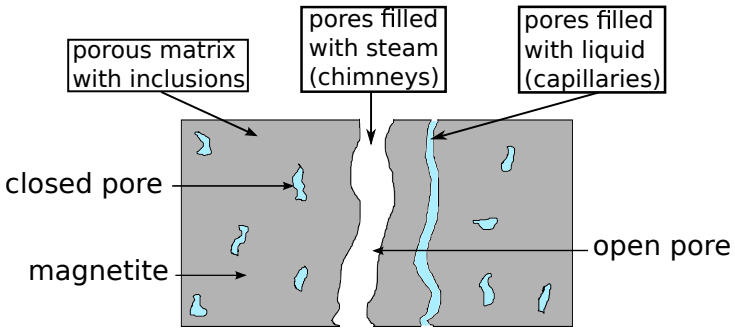

Figure 2: Schematics of the three heat transfer paths

- The porous matrix of magnetite. It is populated with closed pores filled with liquid;
- The capillaries;
- The steam chimneys.

Therefore, the deposit effective thermal conductivity k_{dep} may be expressed as the sum of three thermal conductivities:

$$\begin{aligned} k_{dep}(x)\frac{S_{dep}}{\Delta x} &= k_m(x)\frac{S_m(x)}{L_m(x)} \\ &+ k_l \int_0^{R^*(x)} \frac{1}{L_{op}(R,x)} \frac{\partial S_{op}(R,x)}{\partial R} \mathrm{d}R \\ &+ k_g \int_{R^*(x)}^{+\infty} \frac{1}{L_{op}(R,x)} \frac{\partial S_{op}(R,x)}{\partial R} \mathrm{d}R \end{aligned} \tag{11}$$

The first term of the right hand side of equation 11 corresponds to the thermal conductance of the porous matrix; the second term refers to the thermal conductance of capillaries; and the last term represents the conductance of the steam chimneys. Δx is the thickness of layer x. k_m, k_l, k_g are the thermal conductivity of the matrix, of the capillaries and of the steam chimneys respectively. $L_m(x)$ is the length of the matrix in layer x. $L_{op}(R,x)$ is the length of an open pore of radius R in layer x. For open pores whose shape resembles to straight cylinders aligned in the x-direction, $L_{op}(R,x) = L_m(x) = \Delta x$. For tortuous pores (which

is for a more realistic representation of the porous medium), the tortuosity of the path τ is introduced:

$$\tau_m = \frac{L_m}{\Delta x} \geq 1 \quad \text{and} \quad \tau_{op}(R,x) = \frac{L_{op}(R,x)}{\Delta x} \geq 1 \tag{12}$$

The matrix tortuosity is a function of the open porosity as expressed in Pisani's relation [13]:

$$\tau_m(x) = \frac{L_m(x)}{\Delta x} = \frac{1}{1 - C_{Pis}\phi_{op}(x)} \tag{13}$$

C_{Pis} is a coefficient set equal to 0.75 for a deposit made of mono-dispersed spherical particles (see details in [13]). For open pores, τ_{op} is determined from the statistical fractal methodology (Eq. 30).

The effective thermal conductivity k_m is estimated from a homogenization approach such as Maxwell's model [14]:

$$k_m(x) = k_{mag}\frac{1 - \frac{\phi(x)-\phi_{op}(x)}{1-\phi_{op}(x)}\frac{2\left(k_{mag}-k_l\right)}{k_l+2*k_{mag}}}{1 + \frac{\phi(x)-\phi_{op}(x)}{1-\phi_{op}(x)}\frac{\left(k_{mag}-k_l\right)}{k_l+2*k_{mag}}} \tag{14}$$

Therefore, the effective thermal conductivity $k_{dep}(x)$ of a deposit layer is estimated from equations 2-12-13-14:

$$\boxed{\begin{aligned} k_{dep}(x) = {} & k_m(x)\left(1-\phi_{op}(x)\right)\left(1-C_{Pis}\phi_{op}(x)\right) \\ & + k_l\phi_{op}(x)\int_0^{R^*(x)} \frac{1}{\tau_{op}(R,x)}\frac{\partial\varphi}{\partial R}\mathrm{d}R \\ & + k_g\phi_{op}(x)\int_{R^*(x)}^{+\infty} \frac{1}{\tau_{op}(R,x)}\frac{\partial\varphi}{\partial R}\mathrm{d}R \end{aligned}} \tag{15}$$

When the porosity $\phi(x)$ tends to zero, the deposit conductivity tends to the magnetite conductivity k_{mag}. Similarly, when the proportion of open pores tends to zero, the effect of open pores (filled with liquid or vapor) vanishes and the equation 15 becomes equivalent to Maxwell's model.

3.2. Effective hydraulic permeabilities K_l and K_g

The permeabilities K_l and K_g of a deposit porous layer of thickness Δx and area S_{dep} are defined according to Darcy's law:

$$K_i(x) = \frac{\mu_i Q_i(x) \Delta x}{S_{dep} \Delta P_i(x)} \qquad i = l, g \tag{16}$$

ΔP_i is the pressure loss resulting from a volumetric flow rate Q_i for the length Δx.

The volumetric flow rate $Q_i\left(R, x\right)$ for a Poiseuille flow in an open pore of size R is:

$$Q_i\left(R, x\right) = \frac{1}{8\pi} \frac{\Delta P_i(x)}{\mu_i L_{op}(R, x)} \left(\pi R^2\right)^2 \qquad i = l, g \tag{17}$$

Using equation 2, the total liquid flow rate Q_l through the open pores of the layer is:

$$\begin{aligned} Q_l(x) &= \int_0^{R^*(x)} Q_l\left(R, x\right) \frac{1}{\pi R^2} \frac{\partial S_{op}(R, x)}{\partial R} \mathrm{d}R \\ &= \frac{\Delta P_l(x) S_{dep}}{\mu_l} \frac{\phi_{op}(x)}{8} \int_0^{R^*(x)} \frac{R^2}{L_{op}(R, x)} \frac{\partial \varphi}{\partial R} \mathrm{d}R \end{aligned} \tag{18}$$

The total vapor flow rate Q_g is determined in a similar manner:

$$\begin{aligned} Q_g(x) &= \int_{R^*(x)}^{+\infty} Q_g\left(R, x\right) \frac{1}{\pi R^2} \frac{\partial S_{op}(R, x)}{\partial R} \mathrm{d}R \\ &= \frac{\Delta P_g(x) S_{dep}}{\mu_g} \frac{\phi_{op}(x)}{8} \int_{R^*(x)}^{+\infty} \frac{R^2}{L_{op}(R, x)} \frac{\partial \varphi}{\partial R} \mathrm{d}R \end{aligned} \tag{19}$$

Finally, from the definition of the open pore tortuosity $\tau_{op}(R, x)$ (Eq. 12), the liquid and vapor permeabilities $K_l(x)$ and $K_g(x)$ are determined:

$$\boxed{\begin{cases} K_l(x) = \dfrac{\phi_{op}(x)}{8} \displaystyle\int_0^{R^*(x)} \frac{R^2}{\tau_{op}(R, x)} \frac{\partial \varphi}{\partial R} \mathrm{d}R \\ K_g(x) = \dfrac{\phi_{op}(x)}{8} \displaystyle\int_{R^*(x)}^{+\infty} \frac{R^2}{\tau_{op}(R, x)} \frac{\partial \varphi}{\partial R} \mathrm{d}R \end{cases}} \tag{20}$$

Like the effective conductivity, the permeabilities $K_l(x)$ and $K_g(x)$ are dependent on the microstructural properties of the deposit.

In summary, the deposit properties that must be estimated are the proportion of open pores $\phi_{op}(x)$, the tortuosity of open pores $\tau_{op}(R, x)$ and the cumulative open pore-size distribution $\varphi(R, x)$. The method for estimating these physical properties is presented in the next section. The deposit porosity $\phi(x)$ and the deposit thickness l_{dep} are, on the other hand, inputs to the methodology. These properties may be determined experimentally or by a model for fouling deposition.

4. Fractal characterization of the deposit

The blue histogram in Fig. 3 illustrates the volume fraction of open pores for the fouling deposit inside SG. The volume fraction is obtained experimentally with a mercury porosimeter [15]. This technique uses mercury, a non-wetting fluid, to fill the porous media under increasing pressure. The Laplace's law (Eq. 6) drives the filling of the porous media. As the mercury pressure rises, an increasing number of smaller and smaller open pores are filled with mercury. The difference of volume between two successive pressures and, therefore, between two successive open pore sizes may be inferred, leading to the volumetric distribution shown in Fig. 3.

This method provides an estimate of the porosity for the entire deposit. It says nothing however about the variation of the porosity in the x-direction. Moreover, since mercury is a liquid, it cannot penetrate closed pores. Therefore, this measurement technique is suitable for open pores only.

The histogram of Fig. 3 exemplifies a deposit comprising open pores of two different scales of magnitude. These two scales of magnitude appear to comply to a lognormal distribution: one centered on a radius of 20 μm (scale 1) and another second centered on a radius of 0.5 μm (scale 2). The presence of two scales of magnitude for the open pores is not fortuitous. It results from the

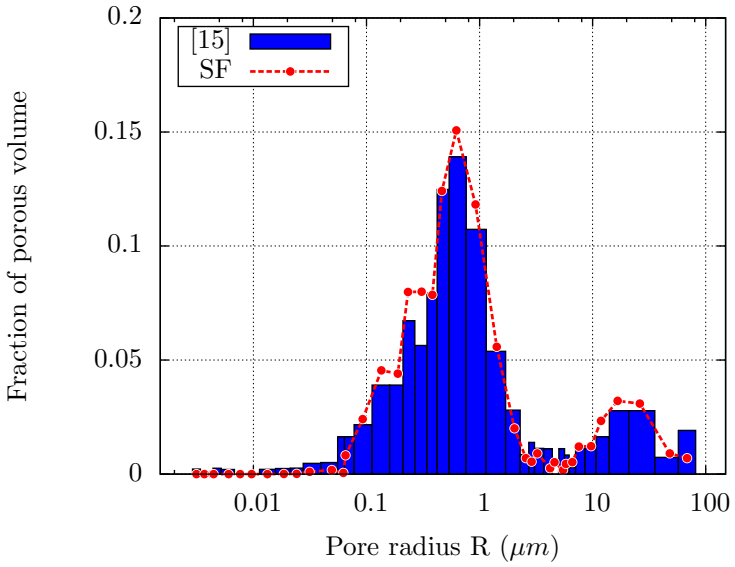

Figure 3: Open pore-size distribution: SF predictions versus Tapping's experimental results [15]

boiling phenomenon that takes place during the fouling deposition. The vapor bubbles produce steam chimneys among capillaries.

Due to the fact that open pores of different scales of magnitude are similar in shape, it is proposed to characterize the fouling deposit with a fractal theory. A fractal is a mathematical object which exhibits similar patterns at several scales [16]. In order to comply with both the statistical lognormal distributions and the fractal behavior of open pores, a novel fractal methodology named "Statistical Fractal (SF)" is developed.

4.1. SF probability density $f(R,x)$

We define the following SF probability density as a sum of n lognormal functions, which share the same standard deviation σ:

$$f(R,x) = \sum_{i=1}^{n} \frac{N_i(x)}{N_{tot}(x)} \frac{\exp\left(-\left(\frac{\ln\left(\frac{R}{R_i}\right)}{\sqrt{2}\sigma}\right)^2\right)}{R\sigma\sqrt{2\pi}} \tag{21}$$

In the case of SG fouling deposits, we have:

- $n = 2$ (capillaries and steam chimneys);
- $N_i(x)$ is the number of open pores of scale i;
- $N_{tot} = \sum N_i(x)$ is the total number of open pores;
- R_i is the median radius of open pores of scale i;

The number $N_i(x)$ of open pores follows the fractal scaling law [16]:

$$\frac{N_i(x)}{N_1(x)} = \left(\frac{R_1}{R_i}\right)^{D_{op}(x)} \Rightarrow \frac{N_i(x)}{N_{tot}(x)} = \frac{R_i^{-D_{op}(x)}}{\sum_{i=1}^{n} R_i^{-D_{op}(x)}} \tag{22}$$

The fractal scaling law is used as a rank-size relation in order to modulate each lognormal distribution. $D_{op}(x)$ is the fractal dimension of open pores. It is obtained from the Rieu and Sposito's fractal model [17]:

$$D_{op}(x) = D_S - \frac{\ln\left(1 - \phi_{op}(x)\right)}{\ln\left(\frac{R_n}{R_1}\right)} \tag{23}$$

D_S is the fractal dimension of roughness for the deposit surface. It is estimated at 2.7 by fitting the theoretical open pore-size distribution with the experimental data (Fig. 3 and section 6.1). As expected, when $\phi_{op}(x)$ tends to 0, $D_{op}(x)$ tends to D_S.

When the total porosity ϕ is known instead of the open pore porosity ϕ_{op}, the latter may be coupled to the former with the Bedrikovetsky's correlation [18]:

$$\phi_{op}(x) = \left\{ \begin{array}{ll} 0, & \text{if } \phi(x) \leq \phi_c \\ \phi(x), & \text{if } \phi(x) \geq 1.65\phi_c \\ 1.65\phi_c \left(\frac{\phi(x) - \phi_c}{0.65\phi_c}\right)^{\beta}, & \text{else} \end{array} \right\} \tag{24}$$

β is a critical exponent, equal to 0.41 for a 3D medium [19]. The percolation threshold ϕ_c corresponds to the minimum porosity value below which the fluid cannot penetrate the deposit. The percolation threshold for a medium composed

of overlapping spheres is equal to 0.2895. [20]. A more accurate value for the percolation threshold could be estimated by comparing the model predictions with experimental data. As the Bedrikovetsky's function shows (Eq. 24), when the porosity $\phi(x)$ drops below ϕ_c, all the pores are closed and $\phi_{op}(x) = 0$. On the other hand, when the porosity is much higher than the percolation threshold, all the pores are open, and consequently, $\phi_{op}(x) = \phi(x)$. In the vicinity of the critical threshold, the percolation theory predicts that the proportion of open pores $\phi_{op}(x)$ is proportional to $(\phi(x) - \phi_c)^{\beta}$ [21].

The present SF methodology employs two open pore scales. However, it may be different for other porous media. It can be shown that if n becomes very large, the prediction of the SF methodology become indistinguishable from that of the classic fractal theory. Therefore, the SF approach may be considered as a generalization of the fractal theory. The lognormal distribution pertaining to each open pore scale reflects the randomness of nature.

Note that for the limiting case $n = 1$, the equation for the probability density $f(R, x)$ remains valid. The fractal relations 22 and 23 become, however, meaningless.

4.2. SF cumulative open pore-size distribution $\varphi(R, x)$

The number density of open pores is given by the SF distribution $f(R, x)$:

$$\frac{1}{\pi R^2}\frac{\partial S_{op}(R,x)}{\partial R} = N_{tot}(x) f(R,x) \tag{25}$$

The open pore-size distribution is obtained from equations 2, 21, 22 and 25:

$$\boxed{\begin{aligned}\frac{\partial \varphi}{\partial R} &= \frac{N_{tot}(x)\pi R^2}{S_{op}(x)} f(R,x) \\ &= \frac{\sum_{i=1}^{n} R_i^{-D_{op}(x)}}{\exp(2\sigma^2)\sum_{i=1}^{n} R_i^{2-D_{op}(x)}} R^2 f(R,x)\end{aligned}} \tag{26}$$

Integration of equation 26 yields the cumulative open pore-size distribution:

$$\boxed{\begin{aligned}\varphi(R,x) &= \int_0^R \frac{\partial \varphi}{\partial R}\mathrm{d}R \\ &= \sum_{i=1}^{n} \frac{\Gamma_i}{2}\left[\mathrm{erf}\left(\frac{\ln\left(\frac{R}{R_i}\right) - 2\sigma^2}{\sqrt{2}\sigma}\right) + 1\right]\end{aligned}} \tag{27}$$

where Γ_i stands for

$$\Gamma_i = \frac{R_i^{2-D_{op}(x)}}{\sum_{j=1}^{n} R_j^{2-D_{op}(x)}} \tag{28}$$

The fitting with Tapping's experimental results is depicted in Fig. 3. For this comparison, the fraction of porous volume ($\Delta\varphi^j = \varphi(R^{j+1}, x) - \varphi(R^j, x)$) is computed from equation 27 using the same sampling as Tapping ($j \in [1; 39]$). The best fit was obtained with $R_1 = 5\ \mu m$, $R_2 = 0.15\ \mu m$ and $\sigma = 0.8$. Due to the fact that the porosity measured by Tapping is an average porosity, the comparison between the SF methodology and Tapping data was carried out for a layer of porosity $\phi = 0.5$.

Fig. 4 shows the open pore-size distribution obtained with Eq. 26. Fig. 5 depicts the corresponding cumulative distributions generated with Eq. 27. The simulations were conducted for two different standard deviations $\sigma = 0.5$ and $\sigma = 0.8$.

4.3. Meniscus radius at the top layer R^*_{dep}

The parameter R^*_{dep} is required for determining the boundary condition for the vapor pressure. It is assumed that boiling drives the deposit porous structure. As a result, the meniscus radius at the top layer R^*_{dep} is set equal to the minimum value between the capillary and the chimney scale distributions (i.e. the two lognormal distributions). The size of this radius is determined from (Fig. 4):

$$\frac{\partial^2 \varphi}{\partial R^2}(R^*_{dep}, l_{dep}) = 0 \quad and \quad \frac{\partial^3 \varphi}{\partial R^3}(R^*_{dep}, l_{dep}) > 0 \tag{29}$$

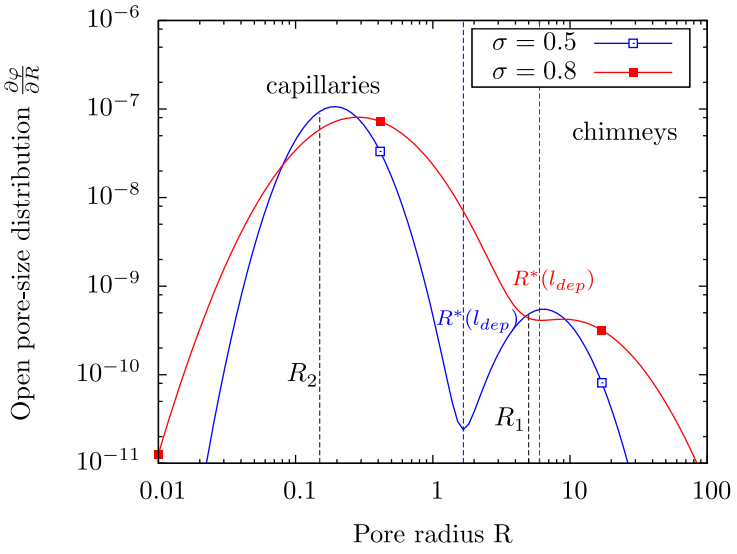

Figure 4: Open pore-size distribution (Eq. 26 with $R_1 = 5\ \mu m$, $R_2 = 0.15\ \mu m$)

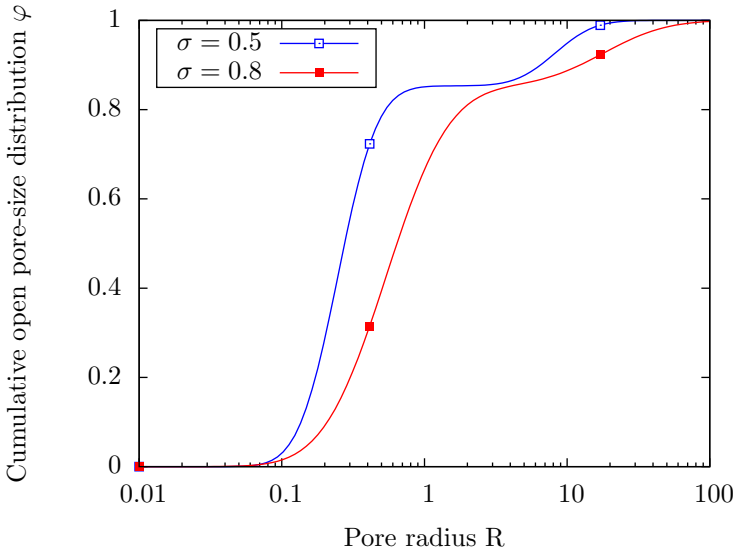

Figure 5: Cumulative open pore-size distribution (Eq. 27 with $R_1 = 5\ \mu m$, $R_2 = 0.15\ \mu m$)

4.4. Open pore tortuosity $\tau_{op}(R,x)$

The fractal theory [22] predicts that the tortuosity of open pores follows the scaling law:

$$\tau_{op}(R,x) = \left(\frac{l_{dep}}{R}\right)^{D_\tau(x)-1} \tag{30}$$

$D_\tau(x)$ is the tortuous fractal dimension and do not depend on R. It may be estimated as [22]:

$$D_\tau(x) = 1 + \frac{\ln\left(\langle\tau_{op}\left(R,x\right)\rangle_R\right)}{\ln\left(\frac{l_{dep}}{\langle R\rangle_R}\right)} \tag{31}$$

The operator $\langle . \rangle_R$ represents an average over the open pore radius R. Using equations 21 and 22, the mean open pore radius $\langle R\rangle_R(x)$ is obtained:

$$\begin{aligned}\langle R\rangle_R(x) &= \int_0^{+\infty} \mathrm{R} f(R,x)\mathrm{d}R \\ &= \exp\left(\frac{\sigma^2}{2}\right)\frac{\sum_{i=1}^n R_i^{1-D_{op}(x)}}{\sum_{i=1}^n R_i^{-D_{op}(x)}}\end{aligned} \tag{32}$$

A tortuosity model from the percolation theory [17] is employed to estimate the averaged open pore tortuosity:

$$\langle\tau_{op}\left(R,x\right)\rangle_R = \left(\frac{\phi(x)-\phi_c}{1-\phi_c}\right)^{\nu\left(1-D_{path}\right)} \tag{33}$$

ν is a universal exponent equal to 0.88 in 3D. D_{path} is the fractal dimension for the optimum path. It is equal to 1.43 in 3D [17]. The tortuosity tends to 1 when the porosity tends to 1. When the porosity $\phi(x)$ approaches the percolation threshold ϕ_c, the tortuosity becomes infinite. Below the percolation threshold, the notion of tortuosity becomes meaningless and the model is no longer valid.

5. Summary of the overall calculation procedure

The above calculation procedure may be summarized as follows:

The input data are:

- The median radii $R_i(x)$ of the n levels of open pores;
- The standard deviation σ of the lognormal distributions;
- The deposit surface fractal dimension D_S;
- The porosity $\phi(x)$ and the percolation threshold ϕ_c.

From these data, the fractal description allows the computation of the following deposit properties:

- The meniscus radius $R^*(x)$ (Eqs. 6 and 29);
- The cumulative open pore-size distribution $\varphi(R, x)$ (Eqs. 21 to 28);
- The open porosity $\phi_{op}(x)$ (Eq. 24);
- The open pore tortuosity $\tau_{op}(R, x)$ (Eqs. 30 to 32).

The thermal-hydraulic parameters are then computed for:

- The volumetric phase change coefficient α_B (Eq. 5);
- The effective deposit conductivity k_{dep} (Eq. 15);
- The liquid and gas permeabilities K_l and K_g respectively (Eq. 20);

Finally, the overall heat transfer coefficient h_{fouled} is determined from equation 1 to 10.

6. Validation

The present paper proposes a novel predictive methodology for the thermal impact of SG fouling which is based on a fractal approach. This approach is unique in the sense that it provides a wealth of information of the porous structure of the fouling deposit. Unfortunately, the scarce experimental data available in the open literature does not provide detailed information. As a result, the present validation will focus on the overall characteristics of the deposit, such as the cumulative open pore-size distribution. First the fractal methodology is validated. Next, the thermal-hydraulic model is confronted to experimental data. Finally, the overall heat transfer model is compared to data provided by the Electric Power Research Institute (EPRI).

6.1. Validation of the fractal description of the deposit

The fractal approach was first validated with the experimental data provided by Uhle [5]. These data were generated from deposit samples that were produced by a sintering process of magnetite particles on SG-tubes. Note that in real situations, the formation of fouling deposits is far more complicated. It involves, for example, corrosion products that are transported by the bulk fluid and settle down on the surface of the SG-tubes for time periods extending to several years, forming deposits of roughly 100 micrometers thick. Also, the boiling phenomenon drives the geometry of the deposits with steam chimneys fed by liquid capillaries. And, due to the precipitation of solute species, the porosity of the deposit layers evolves over time.

Nevertheless, Fig. 6 compares the cumulative open pore-size distribution φ predicted by the SF methodology to Uhle's experimental data. Due to the fact that the sintering process produces a homogeneous porous medium, Uhle's deposit samples are free of steam chimneys. As a result, n was set equal to 1 for the simulation. The SF methodology parameters R_1 and σ were adjusted for a best fit with the experimental data. The normalized root mean square error (NRMSE) is limited to 10% for the worst case scenario (Table 1). Also note that

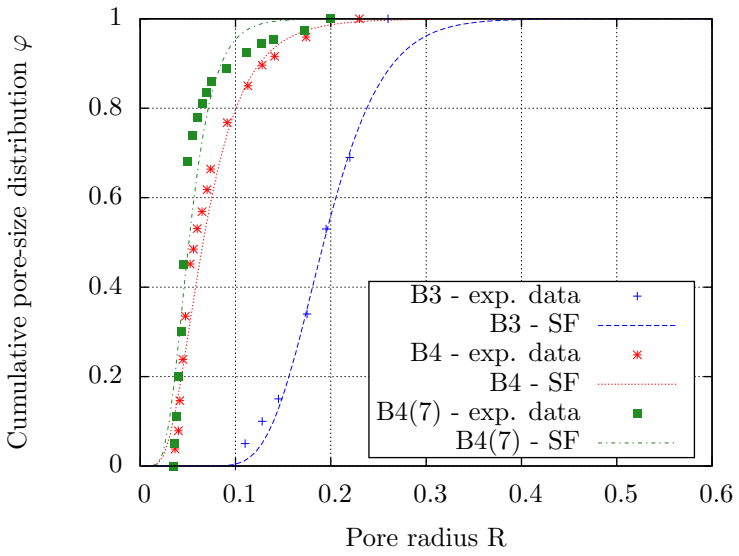

Figure 6: Cumulative open-pore size distribution: SF predictions (Eq. 27) versus Uhle's experimental data [5]

Uhle do not measures these parameters. The validation is carried out with the cumulative open pore-size distribution (Fig. 6). This comparison highlights the suitability of the lognormal function to describe the open-pore size distribution of porous media.

The experimental data provided by Tapping [15] are, on the other hand, closer to reality. The deposit samples were collected from a steam generator of the Chalk River unit 3 [15]. The SF predictions and Tapping's data are compared in Fig. 3. The numerical simulation was conducted for a one-layer constant porosity deposit. The reason is that Tapping's results are available for a mean porosity which is approximately 0.5. This value is beyond $1.65\phi_c \simeq 0.48$. From equation 24, $\phi_{op} = \phi = 0.5$. The median radius R_1 for the open pores of scale 1 (chimney) measured by Tapping is approximately 5 μm. The median radius of open pores R_2 of scale 2 was not, however, measured, nor were the standard deviation σ and the fractal dimension of the deposit surface D_S.

The median radius R_2 of the open pores of scale 2 is estimated at $R_2 = 0.15$

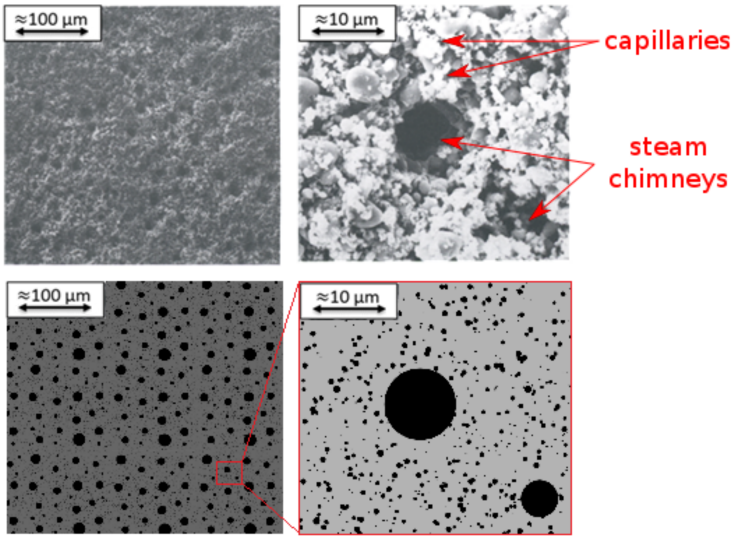

Figure 7: Photographed deposit surface (top) [15]; simulated fouling deposit surface (bottom)

μm by conducting a geometrical inventory of pores on the deposit photograph (topright of Fig. 7).

In order to obtain the σ value, it is assumed that there are no remaining open pores for 3σ decades under R_2, or for 3σ decades over R_1. This assumption yields:

$$3\sigma = \ln(R_2) - \ln(R_{min}) = \ln(R_{max}) - \ln(R_1) \tag{34}$$

R_{min} and R_{max} correspond to the minimum and the maximum open pore-size respectively. The conducted inventory of pores leads to $R_{min} \simeq 0.1R_2$ approximately. The value of the standard deviation $\sigma \simeq 0.8$ is then deduced from Eq. 34.

The magnitude of the D_S parameter is computed by estimating the porosity $\phi_{op}^{(1)} = S_{op}^{(1)}/S_{dep}$ of open pores of scale 1 in Fig. 7. Note that the porosity of open pores of scale 2 is $\phi_{op}^{(2)} = S_{op}^{(2)}/S_{dep} = \phi_{op} - \phi_{op}^{(1)}$. One gets from equation

23:

$$\frac{\phi_{op}}{\phi_{op}^{(1)}} - 1 = \frac{\phi_{op}^{(2)}}{\phi_{op}^{(1)}} = \left(\frac{R_2}{R_1}\right)^{2-D_S+\frac{\ln\left(1-\phi_{op}\right)}{\ln\left(\frac{R_2}{R_1}\right)}} \tag{35}$$

The resulting fractal dimension for the surface roughness is then:

$$D_S = 2 + \frac{\ln\left(\frac{\phi_{op}^{(1)}\left(1-\phi_{op}\right)}{\phi_{op}-\phi_{op}^{(1)}}\right)}{\ln\left(\frac{R_2}{R_1}\right)} \tag{36}$$

The porosity ϕ_{op}^1 of open pores of scale 1 estimated from the 100 μm-scaled photograph (topleft of Fig. 7) is approximately 0.07. Thus, for the given deposit porosity $\phi_{op} = 0.5$, equation 36 predicts $D_S \simeq 2.7$.

Therefore, the estimated parameters $R_2 = 0.15\ \mu m$, $\sigma = 0.8$ and $D_S = 2.7$ yield a good agreement with the measured fraction of porous volume (Fig. 3). The resulting NRMSE is 5.1% (Table 1).

Fig. 7 also suggest a qualitative good agreement since the predicted fouling deposit surface is comparable to Tapping's photograph. This comparison points out the relevance to combine the fractal theory and lognomal functions to depict the porous structure of SG fouling deposits.

6.2. Validation of the modelling of thermal-hydraulic parameters

Fig. 8 compares Uhle's experimental data to the SF predictions for the effective thermal conductivity k_{dep} (Eq. 15). Uhle reported few data for the thermal-hydraulic parameters of the deposits. It is limited to a narrow range of porosities. Fig. 8 shows also the estimates of the Maxwell-Eucken (ME) [14], of the Effective Media (EM) [23], of the Series and of the Parallel model. The experimental data of Uhle are distributed between the EM and the series model.

Fig. 8 reveals that the SF methodology is however the only approach capable of catching the steep change that occurs at the percolation threshold $\phi_c = 0.2895$. Below this threshold, conduction heat transfer prevails. The predictions of the

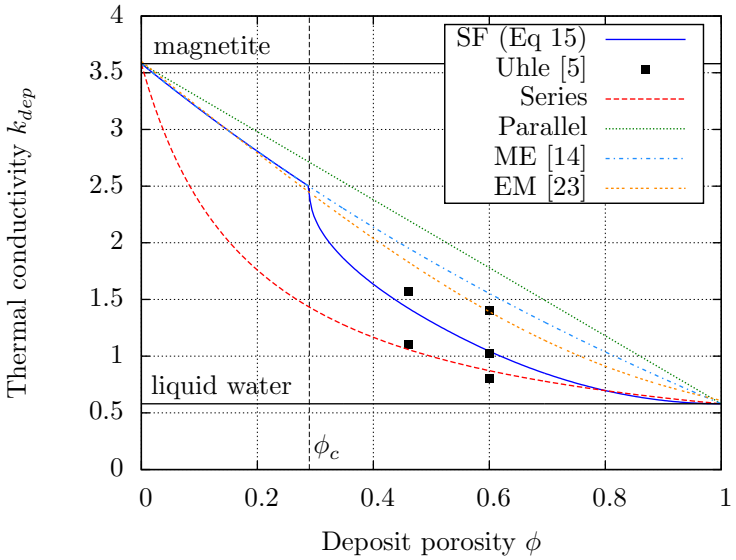

Figure 8: Predicted and measured effective thermal conductivity [5]

SF, of Maxwell-Eucken, and of EM models are all comparable. These models are known to estimate fairly accuretely the thermal conductivity of low porosity media. At the threshold and beyond, boiling dominates heat conduction. The conductivity predicted by the SF methodology falls below that of the EM model and levels off to conductivity values that correspond to a porosity of about 0.7. This behavior is a good indicator of the qualitative trend of the SF methodology. Note that fouling deposits of porosity greater than 0.7 are rarely observed in SGs. Their mesh structure is too fragile to stick to the tube surface. As a result, they are washed away by the bulk fluid stream.

The permeability was examined for single phase flows through different porous materials. These materials include magnetite sintering [5], copper sintering [24] and natural rocks [25]. The predicted and measured effective permeabilities are depicted in Fig. 9. The liquid permeability K_l was estimated with equation 20 for $R^* = \infty$. The median radii of open pores level R_i were estimated for each experiment. When σ is not provided in the data base, it is set equal to 0.4. The SF predictions are, overall, in good agreement with the experimental data.

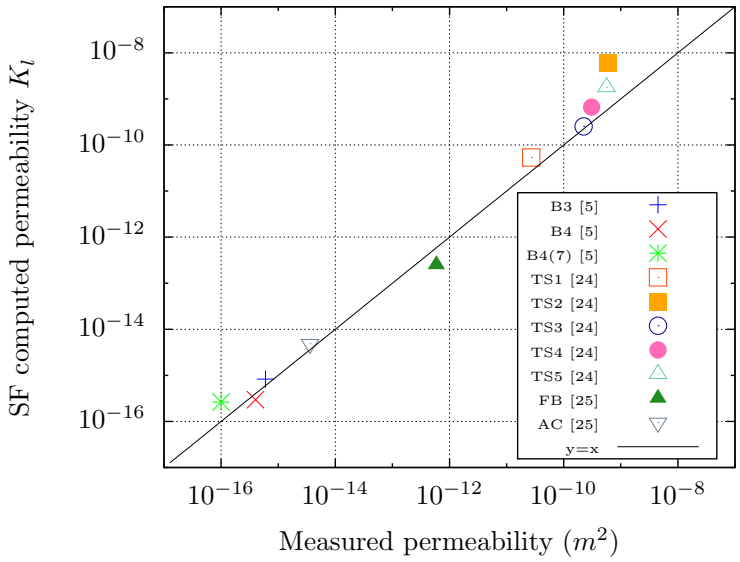

Figure 9: Predicted and measured permeability [5][24][25]

These results also confirm that the lognormal distribution is a suitable choice for depicting a large range of porous media.

6.3. Validation of the overall heat transfer model

The heat transfer model was validated with experimental data extracted from the Chalk-River Unidentified Deposit (CRUD) experimental database of EPRI [26]. This database comprises data for large scale thermal-hydraulic properties of nuclear fuel channels (fluid pressure, cladding temperature T_w , fluid temperature T_∞, mass flow M_∞, heat flux q''_w) as well as data on fouling deposits (porosity ϕ, thickness l_{dep}, radius R_1 of open pores of scale 1). The CRUD database provides however data for at most two layers of deposit. As a result, the SF simulations were carried out for no more than two layers of deposit. Also, the validation reported here rests on the comparison of the predicted and measured overall heat transfer coefficient h_{fouled} defined in equation 1.

Three sub-cooling conditions are available in the CRUD database: $\Delta T_{sub} = 10K$, $18K$ and $55K$. Moreover, the heat transfer regime examined here is

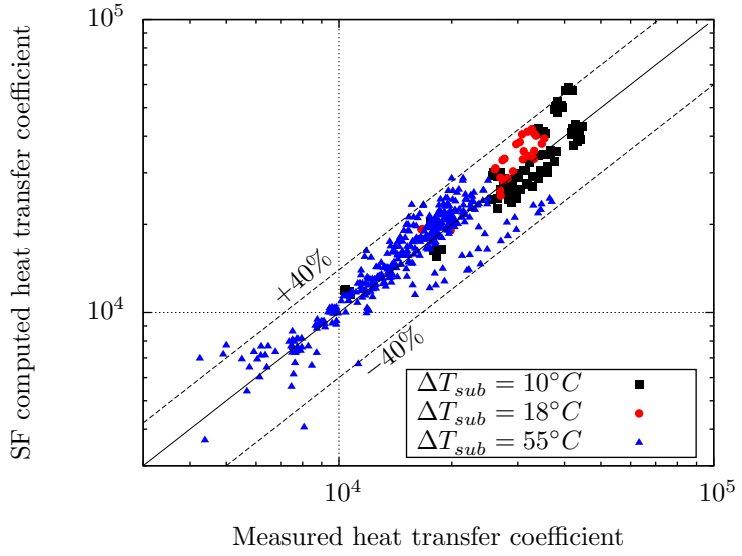

Figure 10: Predicted and measured heat transfer coefficient h_{fouled}

nucleate boiling. The dry-out regime, which rarely occurs in SG, is ignored (Table 2).

Fig. 10 shows that the agreement between the predicted and the measured heat transfer coefficients is very good. Only 2% of the points lie outside the 40% band with a maximal error reaching 98% for the farest point. However, these points are not really representative of the general trend. The Mean Error (ME) on the predicted overall heat transfer coefficient h_{fouled} is estimated at 4.6% and the Mean Absolute Error (MAE) is 11.8%. The present MAE is smaller than the MAE estimated with Uhle's results (17.5%). The MAE also falls well within the margin of uncertainty of the empirical correlations employed for estimating the heat transfer coefficients [9] [10].

7. Results and discussion

Unless explicitly indicated, the following simulations were performed with the thermal-hydraulic and the deposit properties listed in table 3. The deposit is

modeled by assuming a porosity varying linearly:

$$\phi(x) = \frac{\mathrm{d}\phi}{\mathrm{d}x}\left(x - l_{dep}\right) + \phi_{dep} \tag{37}$$

The maximum porosity ϕ_{dep} corresponds to the porosity of the outer layer $x = l_{dep}$. The deposit porosity cannot be less than the minimum porosity ϕ_{min}. The densification process over years is not able to decreasing the porosity below this value. If the value ϕ_{min} is reached at a layer x, all layers below x have a constant porosity ϕ_{min}.

All available porosity measurements on fouling deposit sample indicate that $\phi_{min} \leq 0.3$ and $\phi_{dep} \in [0.3, 0.7]$.

For $\phi > \phi_{min}$, the gradient of porosity $\frac{\mathrm{d}\phi}{\mathrm{d}x}$ is related to the speed of aging of the deposit. To study its impact on the model, this gradient expresses as:

$$\frac{\mathrm{d}\phi}{\mathrm{d}x} = \frac{0.78}{l_{dep}} \tan\left(\arcsin\left(C_{aging}\right)\right) \tag{38}$$

C_{aging} is the aging parameter. A zero slope is obtained for $C_{aging} = 0$. An infinite slope is obtained for $C_{aging} = 1$.

The inner region of constant porosity ϕ_{min} should not be confused with the inner region for which all pores are closed ($\phi \leq \phi_c$). The latter cannot exist if $\phi_c < \phi_{min}$.

Fig. 11 shows the variation of the power density evacuated by boiling heat transfer Π_B and the open porosity ϕ_{op} as a function of the distance x from the tube wall. The power density is calculated with equation 8 and it is normalized with respect to the maximum value Π_B^{max}. The open porosity is estimated from correlation 24. The profile of porosity was set to ($\phi_{min} = 0.05$, $\phi_{dep} = 0.5$, $C_{aging} = 0.5$) with a deposit thickness $l_{dep} = 100\mu m$. This figure reveals that boiling does not occur in zone 1 due to the fact that all the pores are closed ($\phi < \phi_c$). Heat transfer is conduction dominated and, as a result, the temperature gradient across this zone is steep. In zone 2 ($\phi > \phi_c$), the open pores allow boiling to take place. As the porosity increases across the superimposed layers,

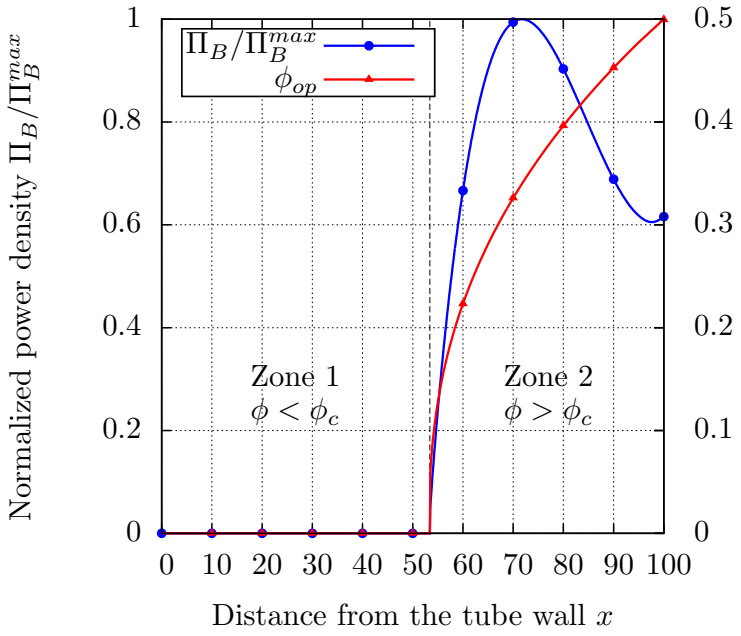

Figure 11: Predicted normalized boiling power density and open pore porosity in a 100 μm-thick deposit ($\phi_{min} = 0.05$, $\phi_{dep} = 0.5$, $C_{aging} = 0.5$)

boiling intensifies and reaches a maximum for $x = 72\ \mu m$. From this point on, boiling diminishes as the temperature difference $T(x) - T_B(x)$ in equation 8 decreases. For thicker deposits, boiling heat transfer keeps decreasing until it completely stops. Heat is then again transferred solely by conduction. In this simulation, the Reynolds number peaked at 0.068 for the vapor phase and 0.013 for the liquid phase. Those values confirm that convection may be neglected in the heat and mass transfer model from Eq. 3 to Eq. 10.

A sensitivity analysis was conducted in order to determine the most influential deposit parameters on the heat transfer. The range for the examined parameters is provided in the third column of table 3. The sensitivity of the deposit thickness l_{dep} was not analyzed since the effect of this parameter is observed on Fig. 13. However, the sensitivity analysis was accomplished with $l_{dep} = 15\mu m$, $l_{dep} = 50\mu m$, $l_{dep} = 100\mu m$, $l_{dep} = 200\mu m$ and $l_{dep} = 300\mu m$. The Sobol sensitivity index was determined from a Monte-Carlo calculation. The 95%

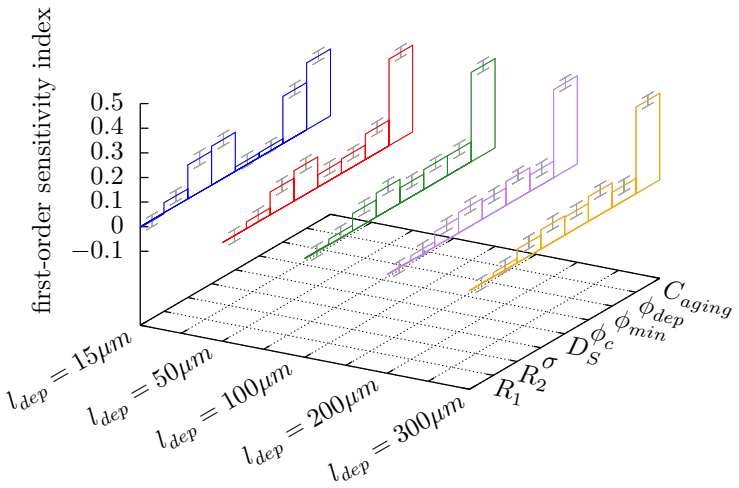

Figure 12: Sobol sensitivity analysis of the SF deposit parameters

confidence interval is also estimated (Fig. 12). Over one million Monte-Carlo simulations were carried out.

It was found that the most influential parameters on the heat transfer coefficient h_{fouled} concerns the profile of porosity: the coefficient of densification ($I_{C_{aging}} \simeq 0.34$), the porosity of the top layer ($I_{\phi_{dep}} \simeq 0.10$) , the minimal porosity ($I_{\phi_{min}} \simeq 0.07$) and the percolation threshold ($I_{\phi_c} \simeq 0.07$). The influence of the coefficient of densification C_{aging} increases with the deposit thickness l_{dep}. Indeed, as the deposit thickness increases, the gradient of porosity applies to a higher thickness and its value take on added importance. The fractal dimension of the surface and the standard deviation have a moderate impact on the heat transfer ($I_{D_S} \simeq 0.11$ and $I_\sigma \simeq 0.08$). The median radius of pores R_i have a negligible effect on the heat transfer ($I_{R_1} \simeq 0.00$ and $I_{R_2} \simeq 0.03$).

Fig. 13 exemplifies the variation of the heat transfer coefficient h_{fouled} in terms of the deposit thickness for aging coefficient C_{aging} ranging from 0 to 1. The minimal and maximal porosity were set to ($\phi_{min} = 0.05$, $\phi_{dep} = 0.5$). It is seen that the smaller the aging coefficient, the larger the heat transfer coefficient. For the limit case $C_{aging} = 0$, boiling takes place in all the deposit: the heat flux conduction tends to zero. In this limit case, an increase of the deposit thickness

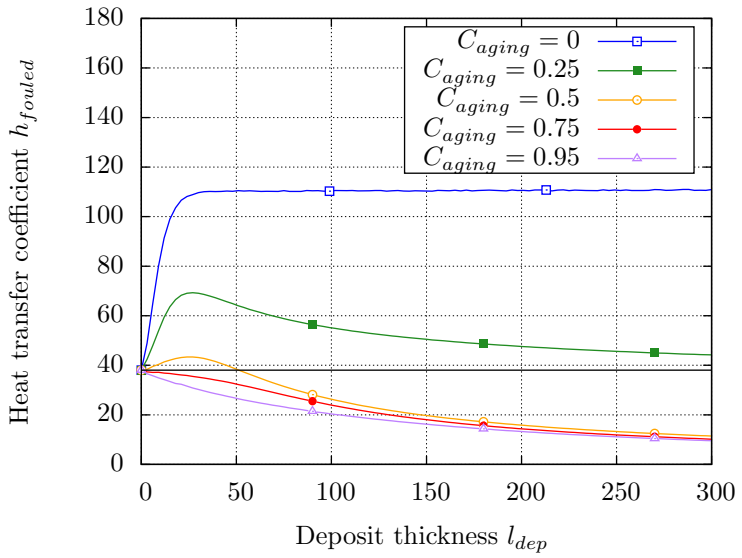

Figure 13: Variation of the heat transfer coefficient with the deposit thickness for several values of C_{aging} ($\phi_{min} = 0.05$, $\phi_{dep} = 0.5$)

has no effect on the heat transfer. For the other cases, the presence of a dense layer with closed pores leads to diminish the heat transfer efficiency when the deposit becomes thicker. This decrease intensifies for high values of C_{aging}.

Fig. 14 shows the variation of the heat transfer coefficient h_{fouled} in terms of the deposit thickness for maximum porosity ϕ_{dep} ranging from 0.3 to 0.7. The minimal porosity and the aging coefficient were set to ($\phi_{min} = 0.05$, $C_{aging} = 0.5$). It is seen that the higher the maximum porosity, the larger the heat transfer coefficient. For low value of ϕ_{dep}, the deposit does not enhance the heat transfer. The thickness of the boiling area in the deposit is too thin to promote the heat exchange. On the contrary, a high enhancement occurs for thin deposits with a high value of ϕ_{dep}.

8. Conclusion

A numerical model was developed for predicting the thermal impact of fouling in steam generators. The novelty of the SF methodology is that it resorts to

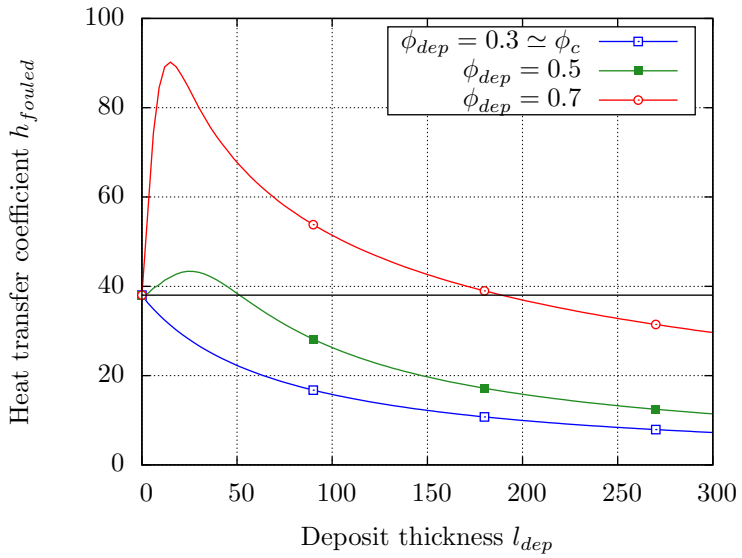

Figure 14: Variation of the heat transfer coefficient with the deposit thickness for several values of ϕ_{dep} ($\phi_{min} = 0.05$, $C_{aging} = 0.5$)

fractal and statistical theories to describe the complexity of the structure of the deposit (the distribution and the tortuosity of pores and the percolation phenomenon) with a limited number of input parameters. The fractal theory reflects the organization between pore scales (capillaries and steam chimneys). The statistical distributions depict the organization in each pore scale.

The present SF methodology considers also fouling deposits as superimposed layers with different values of porosity. Most of the deposit properties evolve according to the deposit layer porosity. It allows to consider the aging mechanisms such as densification which occur during heat exchangers operation.

The proposed model accounts for the heat transfer driven by the liquid-vapor phase change inside the deposits. It simulates the complex intricate networks of sinuous open pores of different scales, with liquid inflows (capillaries) and vapor outflows (steam-chimneys).

The SF methodology was thoroughly validated with experimental data. Concerning the characterization of the porous structure, the SF predictions were

consistent with the available SG fouling data, differing only by 5%. Concerning the prediction of the heat transfer coefficient, a mean absolute error of 12% was made, which is relatively low compared to other heat transfer correlations.

The deposit thickness and the profile of porosity were found to be the most influential fouling properties on the heat exchange. The methodology is capable to simulate the experimentally observed heat transfer enhancement for thin and porous deposit as well as the heat exchange decline for thick and dense deposit.

Most thermal-hydraulic codes employed in the nuclear industry account for the effect of tube fouling by imposing a layer of fixed thickness on the heat transfer surface. The present SF approach allows the strong coupling of the fouling process to the thermal-hydraulic conditions. By strong coupling, we mean that the fouling process is dependent on the flow conditions and, in return, the heat transfer is affected by the resulting deposits. Consequently, the coupling of the SF approach to existing thermal-hydraulic codes may then serve as a predictive tool for managing the cleaning of SG during outages.

The SF methodology shed new light on the way to consider and depict fouling deposits. The approach does not pretend however to elucidate the origin of the porous structure of the deposit. The micro-structural characteristics can only be obtained from the analysis of deposit samples. The physics that governs the deployment of liquid-filled capillaries surrounding steam chimneys is yet to be fully understood. Further experimental investigations are needed in order to develop a general theory for fouling deposition processes that transcends different domains of application. The originality of the fractal approach is to suggest a universal perspective for the construction of a wide range of complex porous structures. As a closing example, Fig. 15 shows that the structural patterns of boiled rice resemble to that of the fouling deposits observed in steam generators of Fig. 7.

Figure 15: Structural patterns generated at the surface of boiled rice

Acknowledgements

This work has benefited from the financial support of Electricité de France (EDF) and of the Association Nationale Recherche Technologie (ANRT). M. Lacroix acknowledges the financial support of the Natural Sciences and Engineering Research Council of Canada (NSERC).

References

[1] P. Cohen, Heat and mass transfer for boiling in porous deposits with chimneys, AlChE Symposium Series 70 (1974) 71–80.

[2] C. Pan, B. Jones, A. Machiels, Concentration levels of solutes in porous deposits with chimneys under wick boiling conditions, Nuclear Enginereering and Design 99 (1987) 317–327. doi:10.1016/0029-5493(87)90130-0.

[3] M. Short, D. Hussey, B. Kendrick, T. Besmann, C. Stanek, S. Yip, Multiphysics modeling of porous crud deposits in nuclear reactors, Journal of

Nuclear Materials 443 (2013) 579–587. doi:10.1016/j.jnucmat.2013.08.014.

[4] D. Yeo, H. NO, Modeling heat transfer through chimney-structured porous deposit formed in pressurized water reactors, International Journal of Heat and Mass Transfer 108 (2017) 868–879. doi:10.1016/j.ijheatmasstransfer.2016.12.046.

[5] J. Uhle, Boiling heat transfer characteristics of steam generator u-tube fouling, Ph.D. thesis, Massachusetts Institute of Technology (1997).

[6] K. Ardon, Micro-caractrisations de l'encrassement des générateurs de vapeur, Mines ParisTech.

[7] S. Klimas, D. Miller, C. Turner, The effect of the removal of steam generator tube ID deposits on heat transfer, AECL Research (1998).

[8] C. Goujon, Consquences des nettoyages chimiques sur la ractivit de la surface externe des tubes de gnrateurs de vapeur des centrales nuclaires racteur eau sous pression, Ph.D. thesis, Université Pierre et Marie Curie (2014).

[9] Z. Liu, R. H. S. Winterton, A general correlation for saturated and subcooled flow boiling in tubes and annuli, based on a nucleate pool boiling equation, International Journal of Heat and Mass Transfer 34 (11) (1991) 2759–2766. doi:10.1016/0017-9310(91)90234-6.

[10] F. Dittus, L. Boelter, Heat transfer in automobile radiators of the tubular type, Journal of Engineering 2.

[11] S. Kovalev, S. Solov'ev, Model of heat transfer in the boiling of liquid at a porous surface, Institute of High Temperatures 22 (6) (1984) 1166–1171.

[12] F.-L. Zhu, K.-J. Li, Fractal analysis of effective thermal conductivity for woven fabrics used in fire fighters' protective clothing, Journal of FIRE SCIENCES 29 (1) (2011) 3–20. doi:10.1177/0734904110371361.

[13] L. Pisani, Simple expression for the tortuosity of porous media, Transport Porous Media 88 (2) (2011) 193–203. doi:10.1007/s11242-011-9734-9.

[14] J. C. Maxwell, A Treatise on Electricity and Magnetism, 3rd edition, Vol. 1 and 2, Dover Publication, 1954.

[15] R. Tapping, C. Turner, R. Thompson, R. Thompson, Steam generator deposits - a detailed analysis and some inferences, Journal of Science and Engineering Corrosion 47 (6) (1991) 489494. doi:10.5006/1.3585283.

[16] B. Mandelbrot, The Fractal Geometry of Nature, W. H . FREEMAN AND COMPANY, 1982. doi:0-7167-1186-9.

[17] A. Hunt, R. Ewing, B. Ghanbarian, Percolation Theory for Flow in Porous Media (3rd edition), Springer, 2014. doi:10.1007/978-3-319-03771-4.

[18] P. Bedrikovetsky, J. Bruining, A percolation based upscaling technique for viscous force dominated waterflooding in uncorrelated heterogeneous reservoirs, in: Proceedings of IOR 1995 - 8th European Symposium on Improved Oil Recovery, EAGE, 1995, pp. 316–326. doi:10.3997/2214-4609.201406986.

[19] A. Stauffer, D. Aharony, Introduction to Percolation Theory (2nd edition), Taylor et Francis, 1992.

[20] M. Rintoul, S. Torquato, Precise determination of the critical threshold and exponents in a three-dimensional continuum percolation model, Journal of Physics A: Mathematical and General 30 (16) (1997) 585–592.

[21] G. R. Grimmet, Percolation, Springer-Verlag, 1989. doi:10.1007/978-3-662-03981-6.

[22] B. Yu, Fractal character for tortuous streamtubes in porous media, Chinese Physics Letters 2. doi:10.1088/0256-307X/22/1/045.

[23] R. Landauer, The electrical resistance of binary metallic mixtures, Journal of Applied Physics 23 (7) (1952) 779–784. doi:10.1063/1.1702301.

[24] Z. Chen, P. Cheng, T. Zhao, An experimental study of two phase flow and boiling heat transfer in bi-dispersed porous channels, Int. Comm. Heat Mass Transfer 27 (2000) 293–302. doi:10.1016/S0735-1933(00)00110-X.

[25] R. Wang, R. Mair, M. Rosen, D. Cory, R. Walsworth, Simultaneous measurement of rock permeability and effective porosity using laser-polarized noble gas nmr, Physical Review E 70 (2). doi:10.1103/PhysRevE.70.026312.

[26] EPRI, Simulated Fuel Crud Thermal Conductivity Measurements Under Pressurized Water Reactor Conditions (2011).

[27] J. R. Varrin, Characterization of PWR Steam Generator Deposits, EPRI (1996).

[28] E. Garboczi, K. Snyder, J. Douglas, Geometrical percolation threshold of overlapping ellipsoids, Physical Review E 52 (1995) 819–828. doi:10.1103/PhysRevE.52.819.

Nomenclature

D_τ	fractal dimension of tortuosity
D_{op}	fractal dimension of open pores
D_{path}	fractal dimension of the optimal path
D_S	fractal dimension of surface roughness
h	heat transfer coefficient, $W.m^{-2}.K^{-1}$
H_B	latent heat of vaporization, $J.kg^{-1}$
K	permeability, m^2
k	thermal conductivity, $W.m^{-1}.K^{-1}$
L	length, m
l	thickness, m
N	number of open pores
n	total number of lognormal distributions
P	pressure, Pa
Q	volumetric flow rate, $m^3.s^{-1}$
q''	heat flux, $W.m^{-2}$
R	radius of open pores, m
R^*	radius of meniscus, m
S	surface, m^2
T	temperature, K
V	Darcy's velocity, $m.s^{-1}$
x	radial distance from the tube wall, m

Greek Letters

α_B	volumetric boiling coefficient, $W.m^{-3}.K^{-1}$
γ	surface tension, $J.m^{-2}$
μ	dynamic viscosity, $Pa.s$
ϕ	porosity
ϕ_c	percolation threshold
Π_B	power density of boiling, $W.m^{-3}$
ρ	density, $kg.m^{-3}$
σ	standard deviation, m
τ	tortuosity
φ	open pore-size distribution

Subscripts and superscripts

∞	secondary bulk fluid (at $x \to +\infty$)
B	boiling
dep	deposit
g	vapor
l	liquid
m	matrix
mag	magnetite
op	open pore
w	SG tube wall (at $x = 0$)

Table 1: SF parameters retained for comparison with Tapping [15] and Uhle [5] results

	Uhle [5]			Tapping [15]
Deposit	B3	B4	B4(7)	CR-3
$R_1(\mu m)$	0.17*	0.04*	0.04*	5
$R_2(\mu m)$	-	-	-	0.15*
σ	0.25*	0.5*	0.4*	0.8*
D_S	-	-	-	2.7*
NRMSE	4.7%	7.1%	9.9%	5.1%

** fitted SF parameters*

Table 2: Selected cases of the CRUD database [26] for the comparison with the heat transfer model

ΔT_{sub} (K)	CRUD case name (-)	Number of data (-)	Rod diameter $2R_{tube}$ (cm)	Heat flux $q_w^{''}$ (MW/m^2)
10	ROD:80,88,91,94	97	0.91/0.95	0.44 - 0.98
18	ROD:110,111	31	0.95	0.49 - 1.16
55	ROD:110,111,112,116,117	381	0.91/0.93/0.95	0.27 - 1.79

Table 3: Physical properties of SG (column 3) and referenced values adopted for the simulations (column 4)

SG	Properties	Range	Simulations
Deposit	l_{dep} (μm)	$\leq$ 300	100
	R_1 (μm)	5 - 10 [27]	5 [15]
	R_2 (μm)	$\leq$ 0.5 [27]	0.15
	σ (-)	0.2 - 0.8	0.8
	D_S (-)	2 - 3	2.7
	ϕ_c (-)	$\leq$ 0.3 [28]	0.2895 [20]
	ϕ_{min} (-)	$\leq$ 0.3	0.05
	ϕ_{dep} (-)	0.3 - 0.7	0.5 [15]
	C_{aging} (-)	0 - 1	0.5
TH	P_∞ (MPa)	5.5 - 7.5	6
	M_∞ $(kg/m^2/s)$	100 - 1000	400
	$q_w^{''}$ (kW/m^2)	100 - 700	200
	Quality (-)	$\leq$ 0.35	0.1